Published in final edited form as:
Phys Med Biol. 2006 October 7; 51(19): 5051–5064. doi:10.1088/0031-9155/51/19/021.

Performance of dedicated emission mammotomography for various breast shapes and sizes

C N Brzymialkiewicz[1,2], **M P Tornai**[1,2], **R L McKinley**[1,2], **S J Cutler**[1,2], and **J E Bowsher**[2]

M P Tornai: martin.tornai@duke.edu

[1]Department of Biomedical Engineering, Duke University, Durham, NC 27708, USA

[2]Department of Radiology, Duke University Medical Center, Durham, NC 27710, USA

Abstract

We evaluate the effect of breast shape and size and lesion location on a dedicated emission mammotomography system developed in our lab. The hemispherical positioning gantry allows ample flexibility in sampling a pendant, uncompressed breast. Realistic anthropomorphic torso (which includes the upper portion of the arm) and breast phantoms draw attention to the necessity of using unique camera trajectories (orbits) rather than simple circular camera trajectories. We have implemented several novel three-dimensional (3D) orbits with fully contoured radius-of-rotation capability for compensating for the positioning demands that emerge from different breast shapes and sizes. While a general orbit design may remain the same between two different breasts, the absolute polar tilt range and radius-of-rotation range may vary. We have demonstrated that using 3D orbits with increased polar camera tilt, lesions near the chest wall can be visualized for both large and small sized breasts (325 ml to 1060 ml), for a range of intrinsic contrasts (three to ten times higher activity concentration in the lesion than breast background). Overall, nearly complete 3D acquisition schemes yield image data with relatively high lesion SNRs and contrasts and with minimal distortion of the uncompressed breast shape.

1. Introduction

Our group has previously developed and investigated a dedicated single photon emission computed tomography (SPECT) system for breast imaging, or dedicated emission mammotomography, utilized with several parallel-beam fully three-dimensional (3D) acquisition orbits about a pendant, uncompressed breast (Archer *et al* 2003, Tornai *et al* 2003, Tornai *et al* 2005a, Brzymialkiewicz *et al* 2005). Key benefits of utilizing 3D acquisition orbits include (1) the ability to contour the breast, reducing distance-dependent spatial resolution limitations, and (2) the capability of imaging further into the breast near the chest wall, by employing camera polar tilt.

Realistic anthropomorphic torso (which includes the upper portion of the arm) and breast phantoms emphasize the necessity of employing unique camera trajectories (orbits) rather than simple circular camera trajectories when collecting projection data. For a simple circular orbit, for example, with 360° azimuthal rotation and no polar camera tilt, the amount of viewable breast volume is limited by the placement of the camera next to the torso and the type of front-end collimator used on the camera. Due to physical limitations, the tissue immediately anterior to the chest wall is not within the field of view (FOV) (figure 1, left, large black arrow) for cameras with parallel collimators. By simply increasing the camera polar tilt angle (φ) to 45°, the centre of the imaging volume moves further into the breast as compared to the simple circular orbit, thus allowing the entire volume to be viewed. However, artefacts result from this particular incompletely sampled orbit. An alternative for potentially increasing the breast imaging volume without using increased polar tilt may

include the use of slant-hole collimators (Baird *et al* 2003, Ball 2003). Breast imaging utilizing slant-hole collimators suffer from a non-uniform resolution due to different distances from the centre of mass of the breast. The average distance of the entire breast is closer using camera tilt than it would be if using a camera without tilt, but having a parallel slant-hole collimator at the same angle as whole camera tilt. Hence, more complex 3D camera trajectories which more-nearly-completely sample the breast while minimizing direct lines-of-sight of the heart and liver are desired. Furthermore, complex 3D orbits can be designed to avoid physical limitations imposed by the patient (e.g. arms) or bed.

Results from previous experiments have shown that no single camera trajectory will equally optimize image quality for various lesion sizes located in different areas of the breast (Archer *et al* 2003, Tornai *et al* 2003, Brzymialkiewicz *et al* 2005). However, some orbits may be more easily adaptable to varieties of breast shapes and sizes. Here, volumetric acquisition orbits that more-nearly-completely sample the pendant, uncompressed breast are investigated, with respect to various breast shapes and sizes. Several orbits are implemented to compensate for the positioning demands that are required for different breast sizes; while a general orbit design may remain the same between two different breasts, the absolute polar tilt range and radius-of-rotation (ROR) range may vary. Thus, orbits are designed with a specific focus on parameters of location of the centre-of-rotation (COR) (and hence viewable breast volume), ROR, and polar tilt angle. The goals of this set of experiments include (1) evaluating the developed orbits with measurements of lesion contrasts and SNRs in anthropomorphic breast phantoms with and without additional torso backgrounds, and (2) examining the effect of various activity concentration ratios and various lesion sizes on image quality, to characterize limitations of the system's performance under different simulated biological conditions.

2. Methods

The dedicated emission mammotomography system we have been developing in our lab has been described in detail elsewhere (Archer *et al* 2003, Tornai *et al* 2003). The compact gamma camera currently attached to the system is the CZT-based LumaGEM 3200-S (*Gamma Medica*, Northridge, CA) with a 60 × 84 array of 2.5 mm^2 discrete pixels. For these studies, the camera incorporates a parallel beam, lead collimator (hexagonally arranged holes, 1.22 mm hole size flat-to-flat, 0.2 mm septa, 25.4 mm height). However, other configurations are possible as collimators are easily interchangeable.

The system was previously evaluated extensively: planar and SPECT performance characteristics of the CZT detector, including system resolution over the expected clinical range, was measured in Brzymialkiewicz *et al* (2005). The camera has a measured mean energy resolution of 6.8% FWHM at 140 keV, and sensitivity of 37.9 cps MBq^{-1} (Brzymialkiewicz *et al* 2005).

2.1. Orbit parameters

For this set of experiments, we focus on three orbit types: vertical-axis-of-rotation (VAOR), which is a simple circular trajectory about a vertical axis and horizontally viewing camera (in whole, resembling rotation about a cylinder); tilted-parallel-beam (TPB), which is a simple, circular trajectory about a vertical axis and obliquely tilted camera (in whole, resembling rotation about a cone); and projected sine wave (PROJSINE), which is a complex, 3D trajectory about a central point having changes in both polar (tilt) and azimuthal orientations simultaneously (in whole, resembling the trajectory of a sinusoid projected onto the surface of a hemisphere).

Within this study, a three-lobed PROJSINE was utilized, though any number of lobes are easily implemented. Three lobes minimized the number of times the camera must reach a polar angle $\varphi = 0°$ (a position requiring larger RORs), while attempting to get around the torso phantom's arm. Two variations of PROJSINE were examined within this work: nearly complete (from $\varphi = 0°$ to $\varphi = 45°$) and incomplete (from $\varphi = 15°$ to $\varphi = 45°$). Nearly complete orbits have been described in detail in Archer *et al* (2003) and Brzymialkiewicz *et al* (2005). If we assume a design criterion meeting Orlov's sampling requirements for more-nearly-complete sampling (Orlov 1975), in that, we force the camera polar tilt angle to reach 0°, the viewable breast volume will be limited (see again figure 1), which could be a significant problem for smaller breast sizes. Thus, we modified the PROJSINE orbits to overcome this potential limitation by sacrificing completeness criterion for the viewable volume, similar to Brzymialkiewicz *et al* (2005). By allowing the camera to start at a polar tilt angle of 15° rather than 0°, the COR also moved farther into the breast.

Parameters for these orbits, including their polar tilt and ROR ranges, are shown schematically in figure 2. Specific orbit parameters used for each scan (details of the set-up are described in the subsequent sections) are given in table 1. VAOR and TPB each had 128 projections; the PROJSINE orbits had 150 projections.

2.2. Isolated breast phantom

Two custom breast phantoms (figure 3 and table 2) (developed for us by *Radiology Support Devices*, Newport Beach, CA) (Tornai *et al* 2005b) were used in conjunction with the 3D orbits. Three lesions were placed in each breast (figure 3): one 0.45 ml (~9.5 mm diam.) catheter balloon lesion (*Harvard Apparatus*, Holliston, MA) was glued with removable rubber cement onto the anterior chest wall; one 0.43 ml (9.4 mm diam.) acrylic sphere lesion (*Data Spectrum Corp.*, Hillsborough, NC) was placed as centrally in the breast as possible; and one 0.26 ml (8 mm diam.) lesion (*Data Spectrum Corp.*) was placed laterally within the breast. The absolute activity for the lesions in the 325 ml breast was 10.6 μCi ml^{-1}; in the 1060 ml breast, the lesion activity was 10.0 μCi ml^{-1}. Note that the dose calibrator in our lab has a ±5% error. The activity concentrations used are higher than that expected clinically in an effort to ascertain the effect of the sampling strategies themselves, which may be most obvious in a set of lower noise images. Twenty minute scans were performed, with acquisition times increased in subsequent scans to account for radioactive decay. A ±8% energy window about the 140 keV photopeak of ^{99m}Tc was used. Three lesion-to-background breast activity concentration ratios were used, including 10:1, 6:1 and 3:1. Once the lesions and breast phantoms were filled, the placement of the lesions remained the same in subsequent scans for different concentration ratios, which were changed by increasing the activity in the background through a small fill port on the side of each phantom.

2.3. Breast phantom with filled torso background

Two activity filled lesions were immersed in the 1060 ml breast phantom, which was then attached to an activity filled anthropomorphic torso phantom that included a heart, lungs and liver (*Radiology Support Devices*) (figures 3 and 4 and table 3). A 1.1 ml (~1.3 cm diam.) lesion was glued to the chest wall; the centre of the lesion was ~1.3 cm anterior to the chest wall, considering the lesion's fill port. In addition, a 2.3 ml (~1.6 cm diam.) lesion (*Radiology Support Devices*) was placed in the centre of the breast (~5.7 cm from the chest wall). The larger, 2.3 ml lesion was used to get a better estimate of the lesion signal (by facilitating a larger region of interest to be drawn within the lesion location) compared to earlier studies with smaller lesions. The absolute lesion activity was 10.4 μCi ml^{-1}; the lesion:torso-and-breast:heart-and-liver activity concentration ratio was 11:1:10. The activity concentrations used are intentionally higher than that expected clinically. Projection data

were acquired for 20 min, with subsequent scans adjusted to compensate for radioactive decay. A ±8% energy window was again used.

2.4. Image reconstruction and ROI analysis

Images were reconstructed from projection data by up to five iterations of ordered subsets expectation maximization (OSEM) with eight subsets (Hudson and Larkin 1994). A ray-driven code was used to accurately model the 3D angles of acquisition within the photon detection probabilities of the OSEM algorithm. Attenuation was modelled through ray-tracing across the attenuating medium, with the linear attenuation coefficient assumed to be 0.12 cm^{-1} within the phantom and 0 cm^{-1} outside. Phantom boundaries were established by first reconstructing the breast without any attention correction, selecting pixel values above a threshold value, then assigning pixels above the threshold a value of 1 and those below a 0. This procedure resulted in a uniform emission mask. The data were then re-reconstructed applying the mask: the values inside the emission mask were assigned the appropriate attenuation coefficient. To summarize the breast-only reconstructed data, maximum intensity projections (MIP) are used because the lesions' locations are on various planes through the breast.

Regions-of-interest (ROIs) were drawn in the reconstructed images both inside the lesions and circumferentially in an annulus about each lesion in the breast background (figure 5). For the breast-only studies, 4-pixel and 9-pixel square ROIs were drawn inside the 0.26 ml and 0.43 ml lesions, respectively. In the breast+filled torso studies, 13-pixel and 25-pixel diamond ROIs were drawn inside the 1.1 ml and 2.3 ml lesions, respectively. The sizes of the ROIs were determined by the diameter of the lesions; ROIs were chosen such that they were completely contained physically within the boundaries of the lesion, centred on the lesions' centroid location. For all studies, annular ROIs were drawn circumferentially about the lesions to determine the background values in the slice containing the lesion, a slice 5 mm above, and a slice 5 mm below. These annular regions contained 216, 264, 348 and 420 total pixels corresponding to the 0.26 ml, 0.43 ml, 1.1 ml and 2.3 ml lesions, respectively.

The signal-difference-to-noise ratio (SNR) was calculated as the difference in mean pixel values of the lesion and breast background, divided by the standard deviation of the uniform background $((ROI_{lesion} - ROI_{breast})/\sigma_{breast})$, where ROI_{lesion} and ROI_{breast} are the mean values of the counts within each respective region and σ_{breast} is the standard deviation of the annular ROI's breast background. Lesion contrast is defined as the signal difference divided by the background signal $((ROI_{lesion} - ROI_{breast})/ROI_{breast})$. As a measure of the homogeneity of the background, the coefficient of variation (CV) or the mean fractional noise is defined as $\sigma_{breast}/ROI_{breast}$ (similar to Graham *et al* (1995), Volkow *et al* (2002)).

3. Results and discussion

As seen in figure 6 (at the dashed black arrow), the lesion nearest the chest wall (0.45 ml) cannot be seen with the VAOR orbit. Similarly, this lesion is not visible for the 1060 ml breast nor the 325 ml breast with VAOR (figures 7 and 8), a result of the physical limitation of placing the detector near the torso (recall figure 1). For the 3:1 concentration ratio, none of the lesions were visible in the 1060 ml breast (figure 7), while all lesions were visible in the 325 ml breast phantom (figure 8) (with the exception of the chest wall lesion using VAOR). This may be expected given the increased ROR with the larger breast and increased amount of attenuating tissue. Considering that we are using a uniform breast background, these results suggest that the system may have increased difficulty in imaging lesions of low radiotracer uptake in larger breast sizes.

Similar to previous results (Tornai *et al* 2003, Archer *et al* 2003, Brzymialkiewicz *et al* 2005), the TPB orbit yields both lesion visualization along with a distorted breast shape due to incomplete sampling (figure 7, dashed black line). Indeed, the lesions are also somewhat distorted with a TPB orbital acquisition. While implementing a TPB orbit is simple and overcomes the volume sampling limitations of VAOR, the distorted image may not ultimately be suitable for clinical use.

The more-nearly-completely sampled PROJSINE orbits recover the breast shape more accurately than TPB; however, artefacts near the chest wall are still visible. Note that there is no activity 'above' the breast volume (i.e. in the chest wall region), yet because of the sampling, in which all activity is not within the FOV for all vantages of the camera, the reconstructed images include incorrectly recovered activity distributions. By sacrificing some polar sampling of PROJSINE by starting at 15° polar tilt rather than 0° (horizon), the COR moves farther into the breast, thus increasing the reduced-artefact region of the breast volume (as artefacts move farther into the breast) and allowing easier visualization of the lesion near the chest wall (figures 7 and 8, black arrows). The circular shape of this chest wall lesion is also more apparent in the PROJSINE 15–45° orbit than the TPB orbit, for both breast sizes.

For the centrally-located 0.43 ml lesion, all orbits yield similar SNR and contrast values for each breast phantom (figure 9) and increase as expected with increasing activity concentration ratio, with the results being higher overall for the 325 ml breast size. Spatial resolution degrades as a consequence of increased ROR. Thus, the higher overall obtained values of SNR and contrast for the 325 ml breast are not surprising given the reduced ROR attainable with the smaller breast size, in addition to its decreased attenuating/scattering volume as compared to the 1060 ml breast. The results also cluster for the 0.26 ml lesion located near the edge of the breast. With only one measurement of each case, the current measurements are likely within error bars (one standard deviation) of each other. Similar studies of the repeatability of these measurements yielded error bars of ~10% on the calculated SNR and contrast values (Brzymialkiewicz 2005).

Images from reconstructed 1060 ml breast+filled torso data are shown in figure 10. Note again the absence of the chest wall lesion in VAOR (figure 10, open black arrows), and the shape distortion of TPB (figure 10, dashed black lines). The larger central lesion facilitated a larger, more reliable ROI estimate; SNR and contrast values for the centrally-located 2.3 ml lesion are given in figure 11. As shown in figure 11, TPB outperforms VAOR, PROJSINE 0–45° and PROJSINE 15–45°. The contrasts for TPB are ~1.4×that of VAOR, reinforcing the importance of close proximity imaging. Furthermore, the orbits that do not strictly follow the sampling criteria for tomographic orbits yield marginally better SNR and contrast values.

In comparing PROJSINE 15–45° to PROJSINE 0–45°, there is an increase in the reduced artefact region of the breast; the artefacts move further into the chest (figure 10, small black arrows). The CV figure-of-merit was used to quantitatively evaluate the effects of the artefacts near the chest wall that result from each orbit. As figure 12 shows, the variability for the centrally-located lesion is minimal. However, in comparison to the centrally-located lesion, the lesion near the chest wall is considerably variable, and is much worse for PROJSINE 0–45° than both TPB 45° and PROJSINE 15–45°. We might expect this result considering the distal artefact lines near the chest wall lesion in the reconstructed PROJSINE 0–45° images.

Of the four classes of orbits studied, the more-nearly-complete orbits yield images that may be more relevant for clinical use. VAOR does not allow imaging near the chest wall. TPB

yields higher SNR and contrast values, but significant shape distortion of both the breast and lesions, which may preclude its clinical use (though this has yet to be determined). The complex PROJSINE orbits yield almost full recovery of the breast's shape. Furthermore, PROJSINE 15–45° has SNRs and contrasts comparable to TPB, almost full recovery of the breast's shape, and visualization of lesions near the chest wall. With less variability near the chest wall as compared to PROJSINE 0–45°, PROJSINE 15–45° may be an optimal orbit type for use in patient studies.

4. Conclusions

Employing 3D data acquisition camera trajectories with increased polar camera tilt, we have demonstrated that lesions near the chest wall can be visualized for both large and small sized breasts for a range of intrinsic contrasts. Because previous studies (Tornai *et al* 2003, Brzymialkiewicz 2005, Brzymialkiewicz *et al* 2005) have suggested that useful, perhaps preferable, images can be obtained from orbits which are moderately shy of complete sampling, we relaxed the restrictions on the camera polar tilt. This allows the COR to move farther into the breast, which increases visualization of lesions near the chest wall. (Please compare PROJSINE 0–45° to PROJSINE 15–45° in figures 7, 8 and 10).

Many metrics may be important in the overall evaluation of sampling strategies, including distortion in reconstructed breast shape, visualization of the volume near the chest wall, total volume that is well sampled, and SNRs and contrasts of test lesions. The present studies were performed somewhat above clinical count densities so that systematic artefacts due to incomplete sampling could be readily observed above the noise. For the breast-only data, all orbits yield very similar SNR and contrast values (figure 9). For the 1.6 cm diameter (2.3 ml) lesion (in the breast+torso studies), PROJSINE 15–45° yields contrast values greater than VAOR (figure 11), attributable to the reduced ROR possible with the PROJSINE 15–45° orbit. Also, PROJSINE 15–45° performed best with the metrics of breast shape, visualization of the chest wall, and total well-sampled volume.

Different sampling strategies could be utilized for different imaging tasks. For example, if a lesion is suspected near the chest wall, then to confirm diagnosis of a lesion in that region, the greater camera tilt and relaxed sampling criteria of the PROJSINE 15–45° orbit might be employed. To determine whether a smaller lesion and/or lesion of low radiopharmaceutical uptake is present anywhere in the breast, an orbit such as TPB, with its decreased ROR, may be initially more appropriate.

The combination of 3D orbits with emission mammotomography yielded images of the smaller 325 ml breast with all three lesions visible, including at the lowest evaluated uptake ratio (figure 8). Furthermore, for the same uptake ratio, the lesions have higher SNRs and contrasts in the smaller breast size than the larger breast size, as a result of the smaller attenuating volume and smaller achievable RORs. Smaller breast sizes are somewhat difficult to image with x-ray mammography, even when the breast tissue is pulled into the imaging FOV. One cause is the difficultly in placing the x-ray detector near the chest wall, similar to the problem of an emission detector collecting data with a VAOR orbit. However, imaging smaller breasts with emission mammotomography and complex orbits does not appear to be a problem, and suggests that this 3D paradigm of imaging the breast may augment mammography for small breast sizes.

Further studies will be necessary to fully characterize the effectiveness of the system for various patient breast sizes, with a non-uniform breast background and variable lesion uptake. Even so, the present studies indicate that our flexible, 3D-positioning emission mammotomography system can achieve nearly complete sampling of large and small

breasts, yielding reconstructed images that have relatively high lesion SNRs and contrasts with minimal distortion of the uncompressed breast shape.

Acknowledgments

The authors thank K Parnham (*Gamma Medica*) for assistance with camera operation. This work was supported by the National Institutes of Health under grants R01-CA096821 and EB001040-01 and by US Army grant no. DAMD17-03-1-0558.

References

Archer CN, Tornai MP, Bowsher JE, Metzler SD, Pieper BC, Jaszczak RJ. Implementation and initial characterization of acquisition orbits with a dedicated emission mammotomograph. IEEE Trans Nucl Sci. 2003; 50:418–20.

Baird WH, Frey EC, Tsui BMW, Wang Y, Wessell DE. Evaluation of rotation slant-hold SPECT mammography using Monte Carlo simulation methods. IEEE Trans Nucl Sci. 2003; 50:105–9.

Ball, G. PhD Thesis. University of Utah; 2003. Multi-segment slant-hole single photon emission computed tomography.

Brzymialkiewicz, CN. PhD Thesis. Duke University; 2005. Development and evaluation of a dedicated emission mammotomography system.

Brzymialkiewicz CN, Tornai MP, McKinley RL, Bowsher JE. Evaluation of fully 3D emission mammotomography with a compact cadmium zinc telluride detector. IEEE Trans Med Imaging. 2005; 24:868–77. [PubMed: 16011316]

Graham LS, Fahey FH, Madsen MT, van Aswegen A, Yester MV. Quantitation of SPECT performance: Report of Task Group 4, Nuclear Medicine Committee. Med Phys. 1995; 22:401–9. [PubMed: 7609720]

Hudson HM, Larkin RS. Accelerated image reconstruction using ordered subsets of projection data. IEEE Trans Med Imaging. 1994; 13:601–9. [PubMed: 18218538]

Orlov S. Theory of three dimensional reconstruction. Sov Phys Crystallogr. 1975; 20:312–4.

Tornai MP, Bowsher JE, Archer CN, Peter J, Jaszczak RJ, MacDonald LR, Patt BE, Iwanczyk JS. A 3D gantry single photon emission tomograph with hemispherical coverage for dedicated breast imaging. Nucl Instrum Methods Phys Res A. 2003; 497:157–67.

Tornai MP, Brzymialkiewicz CN, Bradshaw ML, Bowsher JE, Patt BE, Iwanczyk JS, Li J, MacDonald LR. Comparison of compact gamma cameras with 1.3- and 2.0-mm quantized elements for dedicated emission mammotomography. IEEE Trans Nucl Sci. 2005; 52:1251–6.

Tornai MP, McKinley RL, Brzymialkiewicz CN, Cutler SJ, Crotty DJ. Anthropomorphic breast phantoms for preclinical imaging evaluation with transmission or emission imaging. Proc SPIE. 2005; 5746:825–34.

Volkow ND, Zhu W, Felder CA, Mueller K, Welsh TF, Wang GJ, de Leon MJ. Changes in brain functional homogeneity in subjects with Alzheimer's disease. Psychiatry Res Neuroimaging. 2002; 114:39–50.

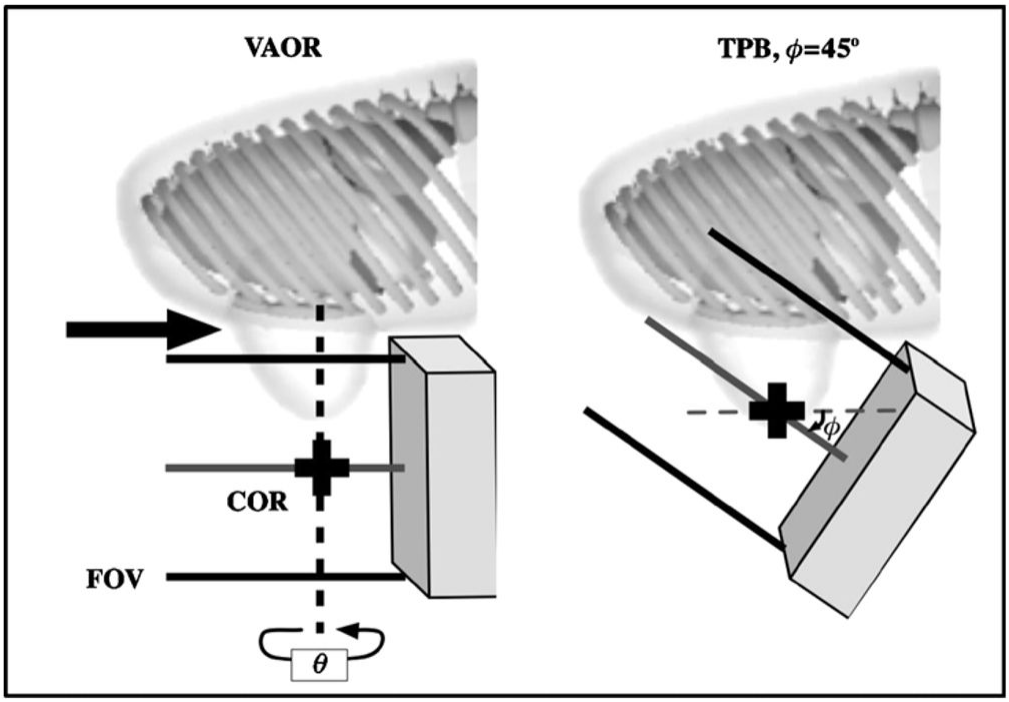

Figure 1.
Simple circular orbits such as a vertical-axis-of-rotation (VAOR) orbit (left) limit the viewable breast volume (large black arrow), due to physical limitations of placing the camera near the torso. The centre-of-rotation (COR) moves further into the breast with increased camera polar tilt (φ) (shown here, e.g., with tilted-parallel-beam (TPB)), allowing for imaging of the breast near the chest wall.

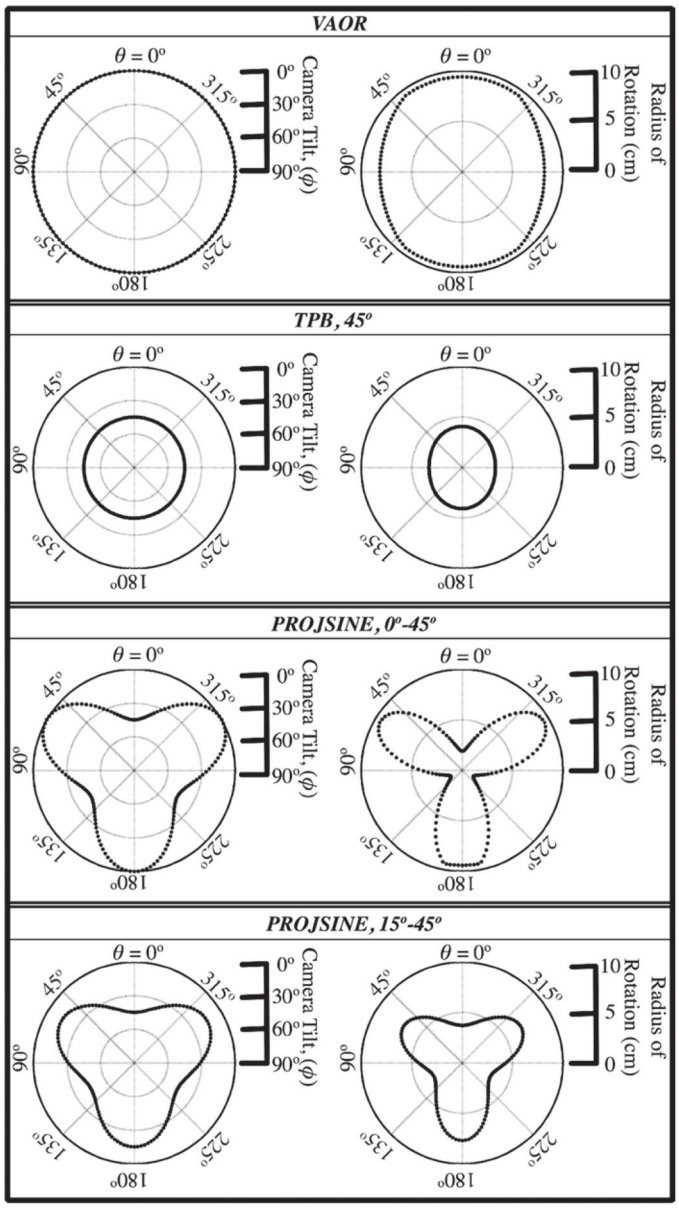

Figure 2.

Within each box, the left plot shows polar camera tilt as a function of the azimuthal angle; the right plot shows the radius of rotation, shown here for the 1060 ml breast phantom.

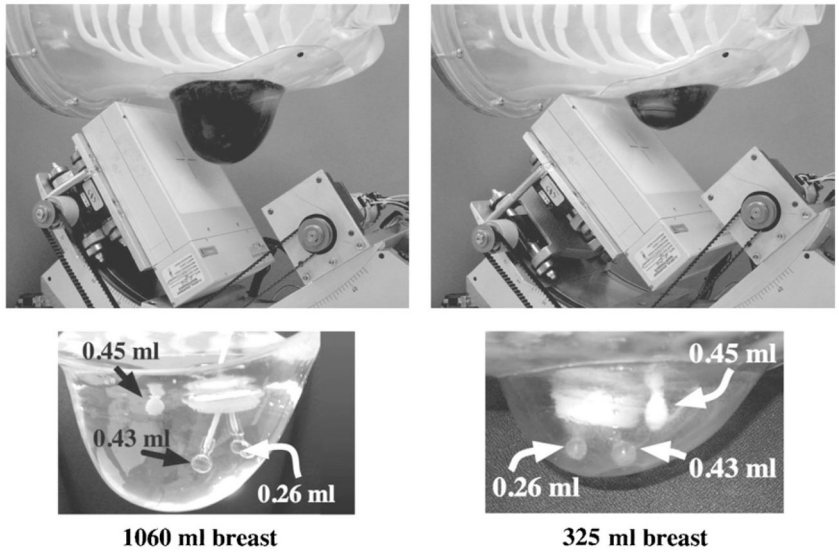

Figure 3.

(Top) Photographs of the 1060 ml (left) and 325 ml (right) anthropomorphic breast phantoms. Note that in the top row of photographs, the breast phantoms have been filled with coloured water to better illustrate the shape and volume differences between these phantoms. Dimensions of the breast phantoms are given in table 2. (Bottom) Three embedded lesions were inserted into each phantom: lesion sizes were 0.26 ml (8 mm diam.), 0.43 ml (9.5 mm diam.) and 0.45 ml (~9.5 mm diam.). The large ring seen is the backside insertion port.

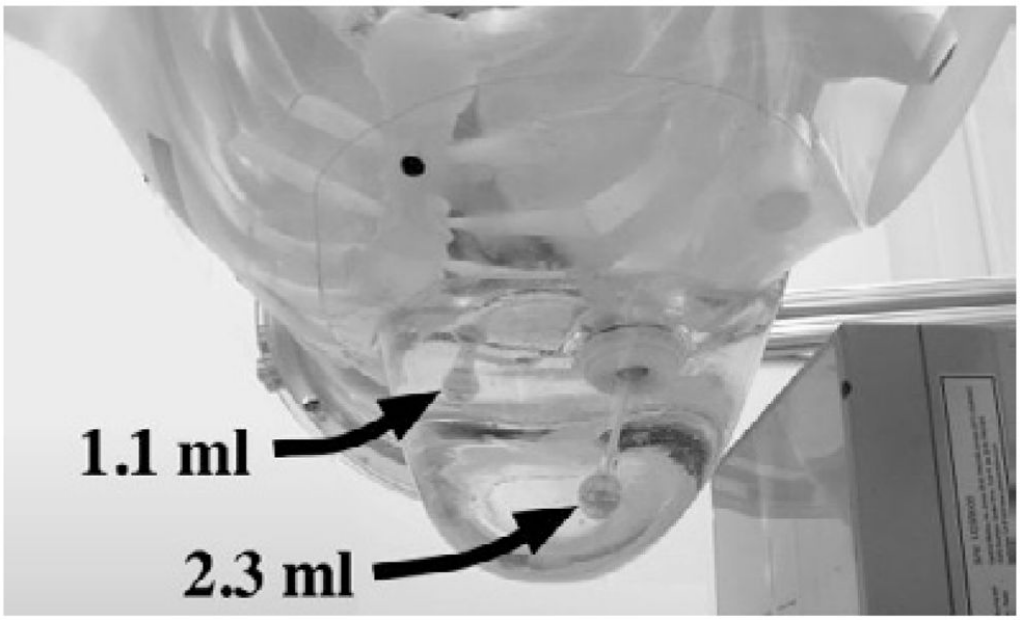

Figure 4.
A photograph of the 1060 ml breast phantom attached to the torso, with two inserted lesions. Lesion sizes were 1.1 ml (~1.3 cm diam.) and 2.3 ml (~1.6 cm diam.).

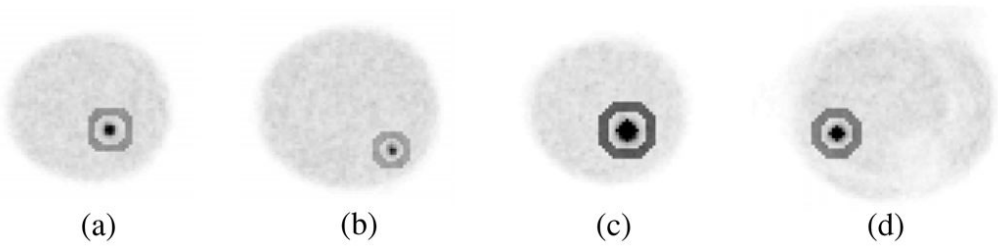

Figure 5.

Example ROIs for (a)–(b) breast-only and (c)–(d) breast+filled torso reconstructed data. (a) 9-pixel square ROI is drawn inside and 264-pixel annular ROI drawn about the centrally-located 0.43 ml lesion; (b) 4-pixel square ROI is drawn inside and 216-pixel annular ROI drawn about the 0.26 ml lesion; (c) 25-pixel diamond ROI is drawn inside and 420-pixel annular ROI drawn about the centrally-located 2.3 ml lesion; (d) 13-pixel diamond ROI is drawn inside and 348-pixel annular ROI drawn about the 1.1 ml lesion.

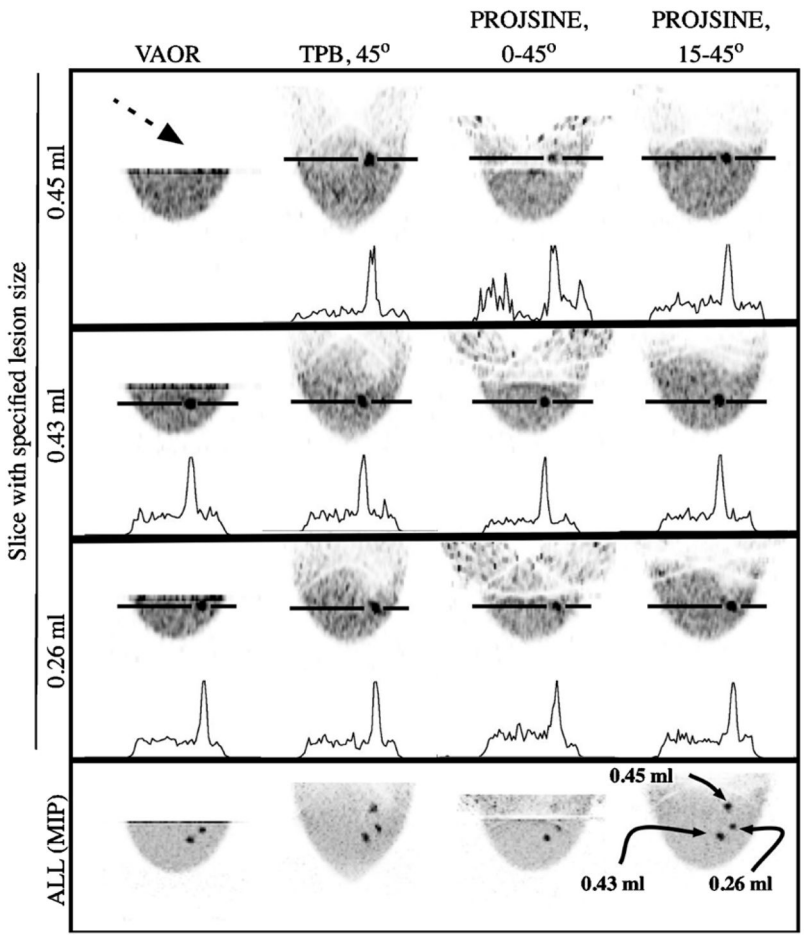

Figure 6.

Top three rows are sagittal images obtained from 1060 ml breast-only reconstructed data (OSEM, 2.5 mm^3 voxels, 2nd iteration shown, calculated attenuation correction, three summed slices to reduce noise) with a 10:1 activity concentration ratio and showing slices containing indicated lesions. Note that the 0.45 ml lesion (located near the chest wall) was not visible with VAOR (dashed black arrow). The bottom row is the maximum intensity projection (MIP) through the breast volume.

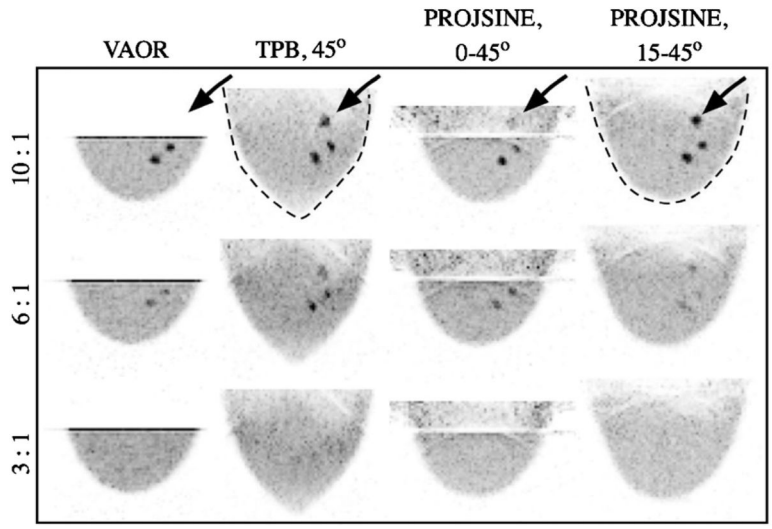

Figure 7.

Maximum intensity projections (sagittal view) for the 1060 ml breast-only reconstructed data for all lesion:breast activity concentration ratios and orbits, as labelled. Black arrows point to the lesion nearest the chest wall, which was most easily visualized with PROJSINE 15–45°. The dashed black line emphasizes distorted and recovered shapes of various orbits. Note that lesions which are not visible in these MIP images are also not visible in their expected individual plane.

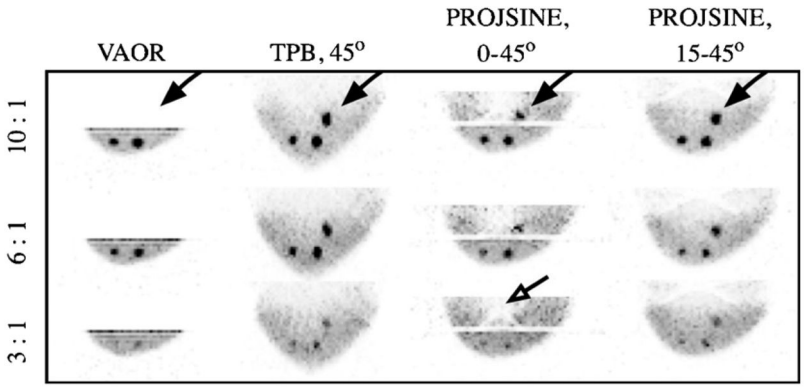

Figure 8.

Maximum intensity projections (sagittal view) for the 325 ml breast-only reconstructed data for all lesion:breast activity concentration ratios and orbits, as labelled. The black arrows point to the lesion nearest the chest wall. The open black arrow points to cold area, due to a nylon screw. Note that all lesions (with the exception of the chest wall lesion in VAOR) are clearly discernible on a computer screen.

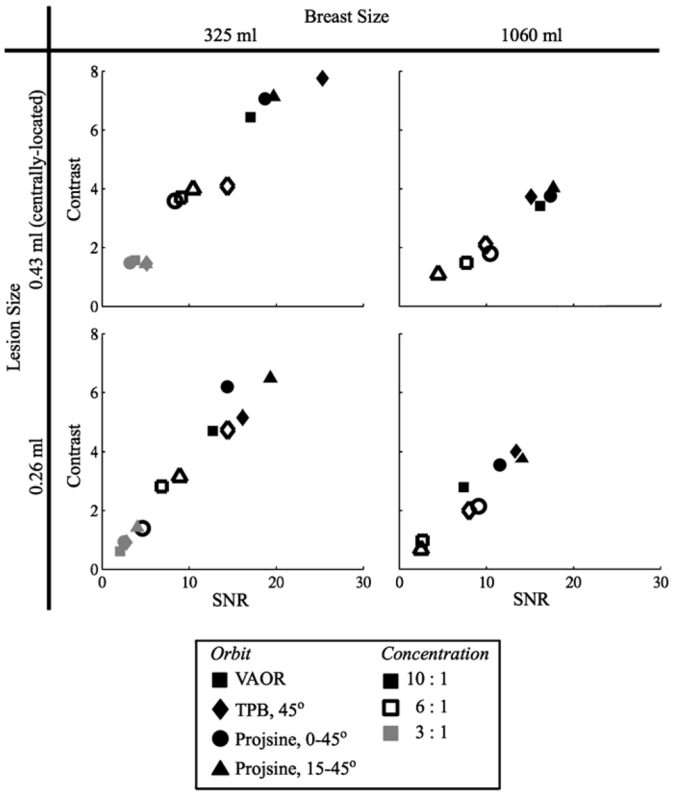

Figure 9.

Contrast versus SNR for the reconstructed 1060 ml and 325 ml breast-only data for the centrally-located 0.43 ml and proximally-located 0.26 ml lesions (2nd iteration only) and for all lesion:breast activity concentration ratios. Note that neither lesion was visible in the 1060 ml breast at a 3:1 ratio.

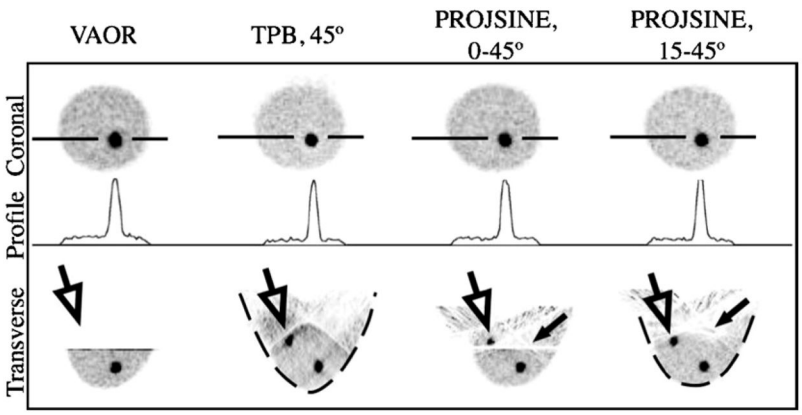

Figure 10.

Images from reconstructed 1060 ml breast+filled torso data (OSEM, 2.5 mm^3 voxels, eight subsets, 2nd iteration shown, calculated attenuation correction, three summed slices to reduce noise, coronal and transverse views as labelled). 3-pixel wide profiles drawn through the 2.3 ml lesion. Similar to the breast-only studies, the lesion near the chest wall (large, open black arrows) is not visible with VAOR, and artefacts (smaller black arrows) move farther into the breast for the PROJSINE 15–45° case as compared to PROJSINE 0–45°. Similar to figure 7, dashed black line emphasizes shape distortion of TPB.

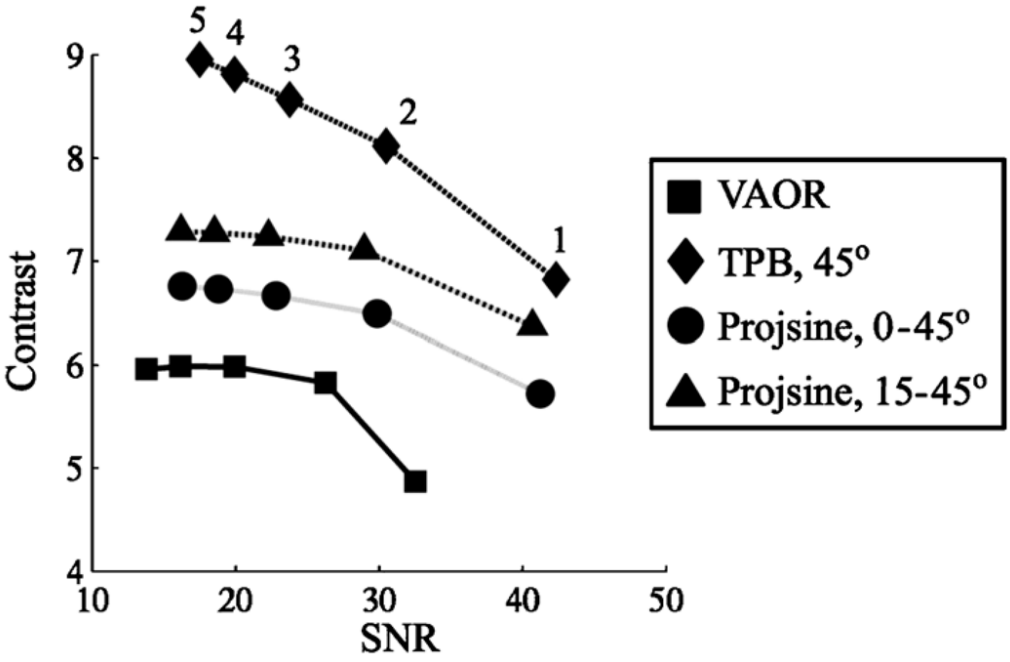

Figure 11.
Contrast versus SNR for the reconstructed 1060 ml breast+filled torso data (11:1:10 lesion:torso-and-breast:heart-and-liver activity concentration ratio) for the centrally-located 2.3 ml lesion. Iteration numbers labelled next to the TPB curve.

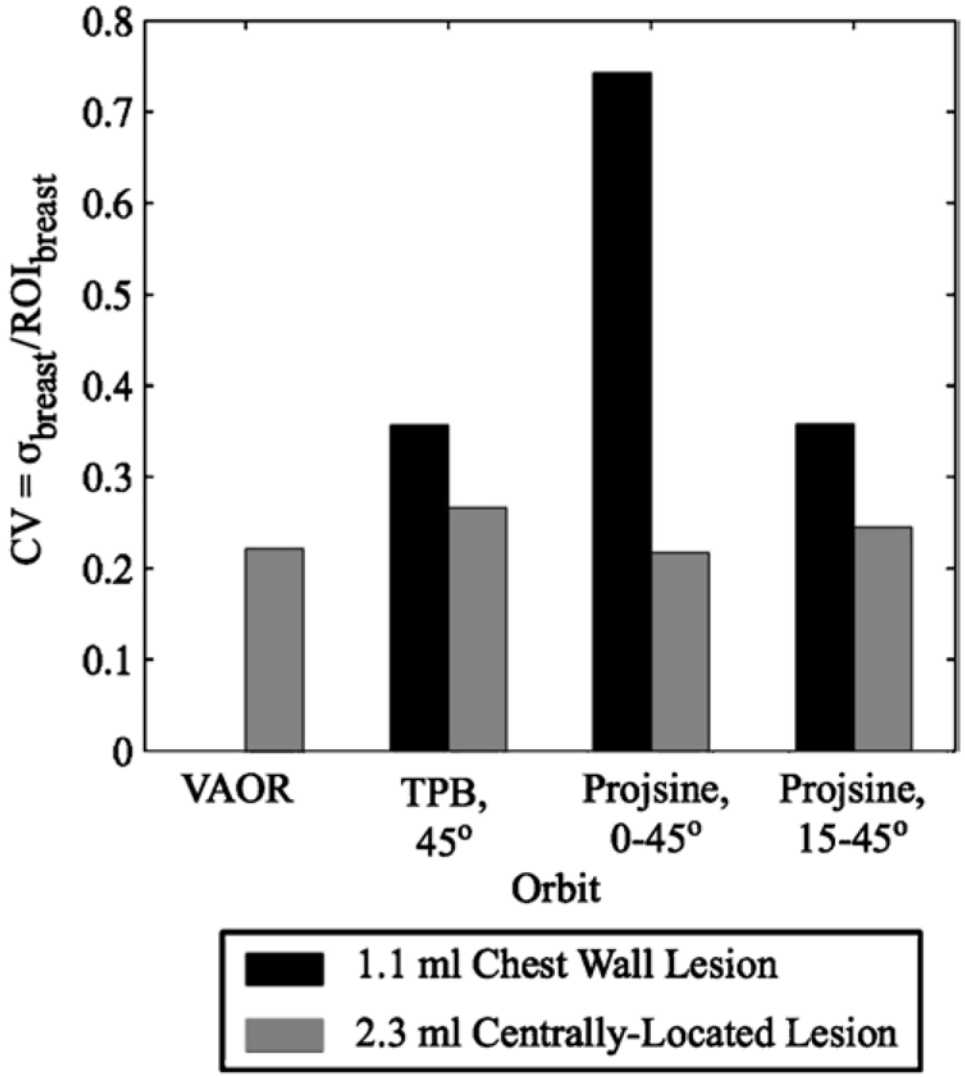

Figure 12.

Coefficient of variation (CV) results for the 1060 ml breast+filled torso data (second iteration only) for the background regions drawn circumferentially about the 2.3 ml centrally-located and 1.1 ml chest wall lesions. Note that a CV value does not exist for the background region about the 1.1 ml lesion with VAOR, as neither the lesion nor the background region about it were visible in the reconstructed data.

Table 1

Parameters used for acquisitions, with all orbits acquired over a 360° azimuthal range (θ).

		325 ml		1060 ml	
Orbit	**Polar tilt (φ)**	**COR[a] (cm)**	**ROR[b] (cm)**	**COR[a] (cm)**	**ROR[b] (cm)**
Breast-only					
VAOR	0°	−5.5	6.1	−1.0	8.0
TPB	45°	−2.6	1.1	1.7	4.0
PROJSINE	0 : 45°c	−5.5	0.0 : 7.0[c]	−1.0	0.8 : 9.4[c]
PROJSINE	15 : 45°c	−2.6	0.6 : 5.5[c]	1.7	3.1 : 7.7[c]
Breast+torso					
VAOR	0°	–	–	−1.0	8.2 : 9.4
TPB	45°	–	–	1.7	3.3 : 4.1
PROJSINE	0 : 45°c	–	–	−1.0	1.3 : 9.4[c]
PROJSINE	15 : 45°c	–	–	1.7	3.1 : 7.7[c]

[a] Location relative to the nipple. Negative values indicate a breast position where the COR is outside and below the nipple. See breast parameters in table 2.

[b] ROR defined as the distance from the centre of the detector to the COR.

[c] Range, minimum:maximum.

Table 2

Dimensions of the distinctly different size and shape custom breast phantoms (*Radiology Support Devices Inc.*).

Breast volume (ml)	Dimensions (in cm)		
	Superior–inferior	Nipple–chest	Medial–lateral
325	12.9	4.4	13.5
1060	16	12	18

Table 3

Volumes and fill concentrations of each of the organs used in the anthropomorphic torso phantom.

Organ	Volume (ml)	Activity concentration (μCi ml^{-1})
Breast	1060	0.95
Torso	7810	0.95
Liver	1010	9.5
Heart (outer wall)	290	9.5
Lesions	1.1	10.4
	2.3	10.4